Chinese Chemical Letters 35 (2024) 109698

Contents lists available at ScienceDirect

Chinese Chemical Letters

journal homepage: www.elsevier.com/locate/cclet

A direct Z-scheme 0D α-Fe_2O_3/TiO_2 heterojunction for enhanced photo-Fenton activity with low H_2O_2 consumption

Cailiang Yue, Nan Sun, Yixing Qiu, Linlin Zhu, Zhiling Du, Fuqiang Liu*

State Key Laboratory of Pollution and Resource Reuse, School of the Environment, Nanjing University, Nanjing 210023, China

ARTICLE INFO

Article history:
Received 18 November 2023
Revised 26 February 2024
Accepted 27 February 2024
Available online 1 March 2024

Keywords:
Photo-Fenton
Z-scheme heterojunction
Chlorophenol
α-Fe_2O_3
TiO_2

ABSTRACT

The insufficient F(III)/Fe(II) cycling rate resulted from high combination of photogenerated carriers severely hinders the photo-Fenton activity. In this work, 0 dimensional α-Fe_2O_3 nanoclusters decorated TiO_2 heterojunction (FT-x) was prepared *via in-situ* phase transformation strategy. FT-200 exhibited the optimal photo-Fenton activity for 2,4-dichlorophenol degradation with the kinetic rate constant reaching 1.0806 min^{-1} under low H_2O_2 dosage (1 mmol/L), which was 126.1 and 202.8 times higher than that of TiO_2 and α-Fe_2O_3. Radical quenching experiments and electron spin resonance spectra proved that ·OH was the leading reactive specie. The enhanced photo-Fenton activity was attributed to the accelerated F(III)/Fe(II) cycling rate induced by the direct Z-Scheme charge transfer mechanism. Benefiting from the abundant ·OH production, the dechlorinate ratios and mineralization ratios of multiple chlorophenol pollutants (2,4-dichlorophenol, 4-chlorophenol, 2,4,6-trichlorophenol) all exceeded 98%. The biotoxicity of chlorophenol wastewater was greatly reduced after the treatment by Light/H_2O_2/FT-200 system. Overall, this work constructed a low-cost and highly efficient photo-Fenton system for refractory organic wastewater treatment.

As one typical kind of the persistent organic pollutants (POPs), chlorophenol pollutants (CPs) have attracted widespread attention due to the potential carcinogenic, teratogenic mutagenic effects and environmental-persistence [1]. Traditional Fenton process has been proved as an efficient technology to decompose refractory organic pollutants by producing abundant ·OH in the presence of Fe^{2+} and H_2O_2 [2]. However, the narrow pH range and huge iron sludge limit its practical application [3]. As a promising alternative, heterogeneous Fenton process is severely restricted by the low Fe(III)/Fe(II) cycling rate and poor stability [4]. In recent years, introducing light in heterogeneous Fenton process, namely photo-Fenton process, can not only boost Fe(III)/Fe(II) cycling rate, but also enhance the stability of catalysts, which has gained extensive attention in recent years [5–7].

Owing to the suitable band gap and low cost, α-Fe_2O_3 is a widely studied photo-Fenton catalyst. However, suffering from high recombination rate of photogenerated carriers, the photo-Fenton activity of simplex α-Fe_2O_3 is rather poor. Constructing heterojunction is an effective strategy to improve the separation efficiency of photogenerated carriers by forming built-in electric field in the interface of heterojunction [8–10]. As one of the most studied photocatalysts, TiO_2 keeps the enduring appeal to researches due to the easy availability, non-toxicity, inexpressiveness and chemical stability [11–13]. However, TiO_2 can only utilize ultraviolet, which greatly constrict the photocatalytic efficiency. Combining TiO_2 with good visible light responsive semiconductor could greatly address these problems. For example, Zeng-Hui Diao *et al.* construct TiO_2/nZVI heterojunction with enhanced photocatalytic persulfate activation for simultaneous degradation of amoxicillin and norfloxacin amoxicillin and norfloxacin [14]. Hence, combining TiO_2 with α-Fe_2O_3 to construct TiO_2/α-Fe_2O_3 heterojunction can not only improve the visible-light harvesting, but also accelerate Fe(III)/Fe(II) cycling rate, thus realizing high H_2O_2 activation. However, due to the existence of severe lattice mismatch between TiO_2 and α-Fe_2O_3, it is challenging to construct effective contact interface [15–17]. Considering both FeOOH and anatase TiO_2 belong to the tetragonal system, TiO_2/α-Fe_2O_3 heterojunction could be obtained by the *in-situ* transformation of TiO_2/FeOOH heterojunction.

Based on the above considerations, 0D α-Fe_2O_3 nanoclusters were loaded on the surface of TiO_2 nanoparticles (FT-x) by *in-situ* calcination of TiO_2/FeOOH heterojunction, which were applied in the photo-Fenton degradation of CPs. Detailed structural characterizations were performed to confirm the successful preparation of FT-200. The photocatalytic H_2O_2 activation and 2,4-dichlorophen (2,4-DCP, a common CPs as the model pollutant) degradation per-

* Corresponding author.
E-mail address: lfq@nju.edu.cn (F. Liu).

https://doi.org/10.1016/j.cclet.2024.109698
1001-8417/

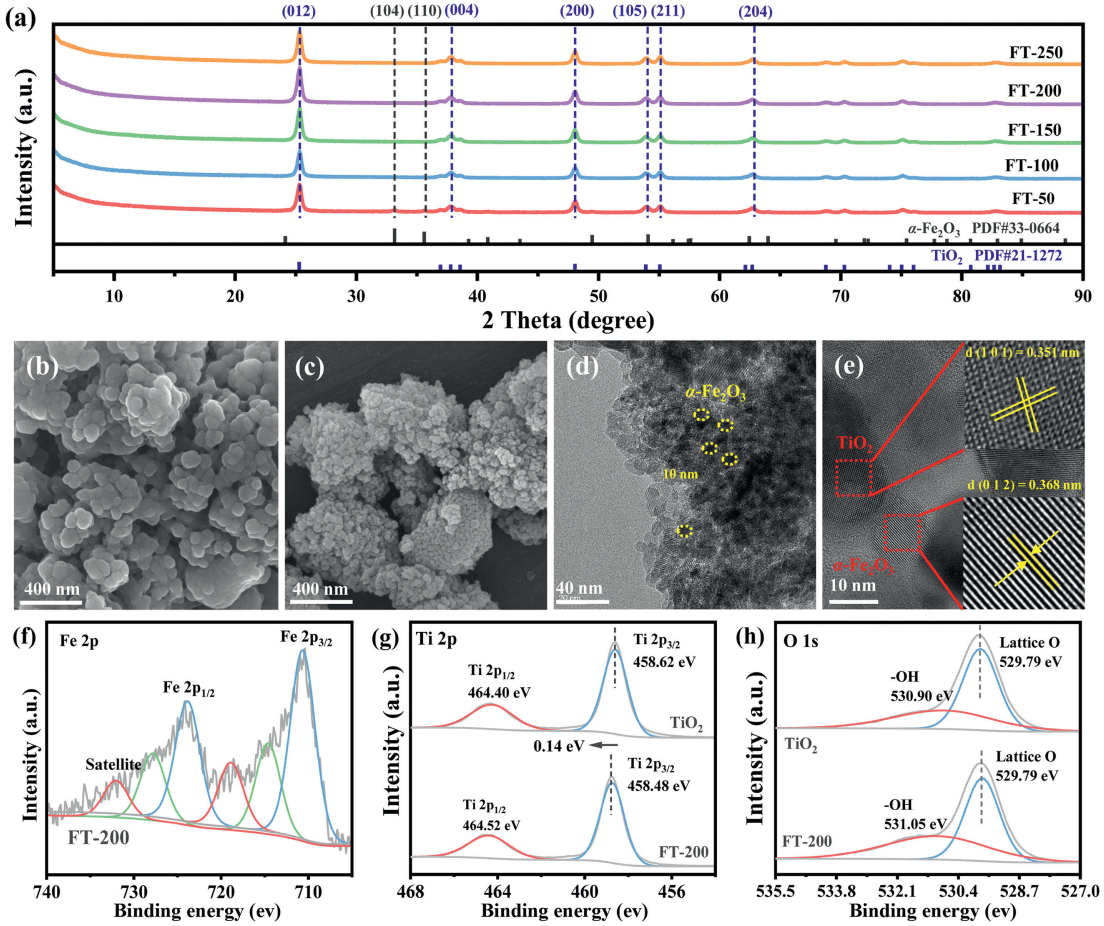

Fig. 1. (a) XRD patterns of TiO_2, α-Fe_2O_3 and FT-x, SEM images of (b) TiO_2 and (c) FT-200. (d, e) TEM images of FT-200 with different scale bars. High-resolution XPS spectra of (f) Fe 2p, (g) Ti 2p and (h) O 1s, respectively.

formances were systematacially evaluated. Quenching experiments and electron paramagnetic resonance (EPR) analyses were conducted to identify the dominated reactive species for 2,4-DCP degradation. The degradation pathway of 2,4-DCP was proposed and toxicity of intermediate products was also evaluated. Overall, this work constructed an effective photo-Fenton system for efficient CPs wastewater treatment.

The crystal structure and chemical composition of FT-x were analyzed by X-Ray diffraction (XRD). As shown in Fig. 1a, the characteristic diffraction peaks appeared at 25.3°, 37.8° and 48.0°, corresponding to the (012), (104) and (200) crystal planes of the anatase TiO_2, respectively [18]. While the two diffraction peaks located at 33.2° and 35.6°, which corresponded to the (104) and (110) crystal planes of α-Fe_2O_3, respectively [19]. This indicated that the α-Fe_2O_3 and TiO_2 coexisted in the crystalline structure of FT-x.

The microstructures of TiO_2 and FT-200 were revealed by scanning electron microscope (SEM) and transmission electron microscope (TEM) images. Pristine TiO_2 showed irregular nanoparticle structure with smooth surface (Fig. 1b). FT-200 maintained the original nanoparticle structure of TiO_2 while the surface became rougher, which was attributed to the *in-situ* loading of α-Fe_2O_3 nanoclusters (Fig. 1c). The TEM image of FT-200 in Fig. 1d further showed that the particle size of α-Fe_2O_3 nanoclusters anchored to its surface were about 10 nm, implying the successful formation of 0D structure. In addition, the lattice spacing of 0.351 and 0.368 nm (Fig. 1e), corresponded to (101) and (012) crystal plane of anatase TiO_2 and α-Fe_2O_3, respectively [13,20]. The energy dispersive spectrometer (EDS) mappings in Fig. S1a (Supporting information) showed that the elements Fe, Ti, and O were uniformly distributed on the surface of FT-200, indicating the successful preparation of heterojunction. The specific surface area, total pore volume and average pore size of the catalysts were also listed in Table S1 and Fig. S2 (Supporting information). It could be found that pristine TiO_2 possessed typical mesoporous structure. The loading of α-Fe_2O_3 nanoclusters on TiO_2 could produce more porosities, which was conducive to the exposure of active sites.

The elementary compositions and valence states were further analyzed by X-ray photoelectron spectroscopy (XPS). The characteristic peak of Fe 2p in the XPS survey spectrum of FT-200 indicated the successful decoration of α-Fe_2O_3 (Fig. S1b in Supporting information). As shown in Fig. 1f, the characteristic peaks of Fe 2p located at 710.8 eV and 724.2 eV corresponded to Fe $2p_{3/2}$ and Fe $2p_{1/2}$, respectively [21], which certified the successful loading of α-Fe_2O_3. The two characteristic peaks appeared at 458.6 eV and 464.3 eV in Ti 2p XPS spectrum of TiO_2 corresponding to Ti $2p_{3/2}$ and Ti $2p_{1/2}$, respectively (Fig. 1g). However, the Ti 2p characteristic peak of FT-200 was shifted by 0.14 eV towards high binding energy, indicating that the loading of α-Fe_2O_3 reduced the electron cloud density in the vicinity of TiO_2 thus leading to the tendency of e^- to migrate towards the surface of α-Fe_2O_3 [22]. The fine spectrum of the O 1s of FT-200 was convolved into two peaks at 529.9 and 531.2 eV, corresponding to the hydroxyl groups and lattice oxygen species, respectively (Fig. 1h).

The band structures of as-prepared samples were determined by ultraviolet-visible diffuse reflectance spectra (UV–vis DRS) and

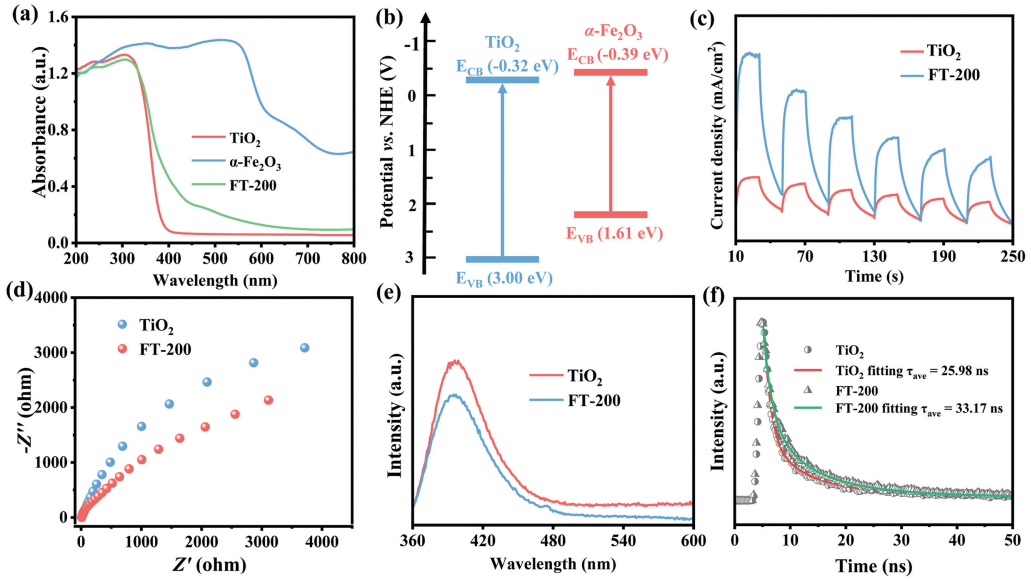

Fig. 2. (a) Tauc-Plots of TiO_2, α-Fe_2O_3 and FT-200. (b) A schematic illustration of band structure of pristine TiO_2 and α-Fe_2O_3. (c) Photocurrent spectra, (d) EIS Nyquist plots, (e) steady-state PL spectra of TiO_2 and FT-200. (f) Time-resolved PL spectra of TiO_2 and FT-200.

Mott-Schottky spectra. As depicted in the UV–vis DRS (Fig. 2a), TiO_2 showed negligible adsorption ability to visible light, while α-Fe_2O_3 exhibited strong light absorption for both UV and visible light. It was worth noting that the absorption peak of FT-200 showed a significant red shift compared with that of pristine TiO_2, which was attributed to the α-Fe_2O_3 nanocluster located on the surface of FT-200. According to the Tauc-plot in Fig. S3 (Supporting information), the energy bandgaps (E_g) of TiO_2 and α-Fe_2O_3 were calculated as 3.32 and 2.02 eV, respectively. The conduction band potentials (E_{CB}) of TiO_2 and α-Fe_2O_3 were measured as −0.32 and −0.43 V based on the Mott-Schottky spectra in Fig. S4 (Supporting information). Then, the valence band potentials (E_{VB}) of TiO_2 and α-Fe_2O_3 were calculated as 3.00 and 1.61 V, respectively. The energy band structures of TiO_2 and α-Fe_2O_3 were presented in Fig. 2b. It was not difficult to show that the formation of heterojunction between TiO_2 and Fe_2O_3 will form a built-in electric field, which was favorable for the separation of photogenerated carriers.

The separation of photogenerated carriers was analyzed by photoelectrochemical measurements. As shown in Fig. 2c, FT-200 displayed a higher photocurrent intensity compared with that of TiO_2, indicating a higher separation efficiency of photogenerated carriers [23]. The electrochemical impedance spectra (EIS) in Fig. 2d showed that FT-200 possessed the smallest semicircle, suggesting the reduced migration resistance for photoexcited e^- in FT-200 [24]. To further investigate the migration kinetics of photogenerated carriers, both the steady-state photoluminescence (PL) and transient-state PL measurements were operated. As shown in Fig. 2e, the PL emission intensity of FT-200 was much lower than that of TiO_2, which meant that the recombination rate of photogenerated carriers in FT-200 was greatly suppressed [25]. According to the PL decay spectra in Fig. 2f and Table S2 (Supporting information), the average fluorescent life of FT-200 was calculated as 33.17 ns, which was longer than that of TiO_2 (25.98 ns), confirming the higher separation efficiency of photogenerated carriers in FT-200 [26]. All of these measurements confirmed that the construction of α-Fe_2O_3/TiO_2 heterojunction could effectively improve the adsorption of visible light and separation of photogenerated carriers.

The photo-Fenton activity of as-prepared samples was systematically evaluated with 2,4-DCP as the model pollutant. As shown in Figs. 3a and b, pristine TiO_2 and α-Fe_2O_3 exhibited poor photo-Fenton activity with the reaction kinetic constant (k) of 0.0085 and 0.0053 min^{-1}, respectively, owing to the high recombination rate of photogenerated carriers. For FT-x, the photo-Fenton activity was greatly promoted, which was attributed to the fast Fe(III)/Fe(II) cycling rate resulting from the improved separation of photogenerated carriers. FT-200 exhibited the optimal photo-Fenton activity with the corresponding k value reached 1.0806 min^{-1} (Fig. S5 in Supporting information), which was 126.1 and 202.8 times higher than that of TiO_2 and α-Fe_2O_3. In addition, the k value of 2,4-DCP degradation in Light/H_2O_2/FT-200 system was 52.2 and 719.4 times higher than that of Light/FT-200 and H_2O_2/FT-200 system, respectively, further confirming the synergistic effect between photocatalysis and Fenton-like process. The leaching iron was determined as only 0.589 mg/L. As depicted in Fig. S6 (Supporting information), the 2,4-DCP degradation kinetics of homogeneous Light/Fe^{3+}/H_2O_2 system was only 0.0122 min^{-1}, which was 1.13% as more as that of Light/H_2O_2/FT-200 system, excluding the crucial contribution of leaching iron.

In the meanwhile, the H_2O_2 decomposition ratio in Light/H_2O_2/FT-200 system achieved 0.0826 min^{-1}, which was 13 times higher than that of H_2O_2/FT-200 system, which implied that the introduction of light could boost Fe(III)/Fe(II) cycling and H_2O_2 decomposition. As shown in Fig. 3c and Tabble S3 (Supporting information), FT-200 possessed an apparent advantage over reported photo-Fenton photocatalysts [27–31]. FT-200 also displayed excellent degradation performance towards other phenolic pollutants, including 4-chlorophenol (4-CP), 2,4,6-trichlorophenol (2,4,6-TCP), phenol and bisphenol A (BPA), with the degradation ratios all reaching 100% within 12 min (Fig. 3d and Fig. S7 in Supporting information). Furthermore, the dechlorination ratios of 4-CP, 2,4-DCP and 2,4,6-TCP by the Light/H_2O_2/FT-200 system reached up to 100.0%, 98.9% and 100%, respectively, and the corresponding TOC removal ratios achieved 91.8%, 91.5% and 96.6% within 30 min, respectively (Fig. 3e).

The effects of initial pH and coexisting substances on 2,4-DCP degradation were investigated to evaluate the practical applicability of Light/H_2O_2/FT-200 system (Fig. S8 in Supporting information). With the initial pH ranging from 3 to 7, there was no distinct fluctuation on TC degradation efficiency, indicating the high pH adaptability. As showed in Fig. S9 (Supporting information), the pH value declined clearly after photo-Fenton reaction, which re-

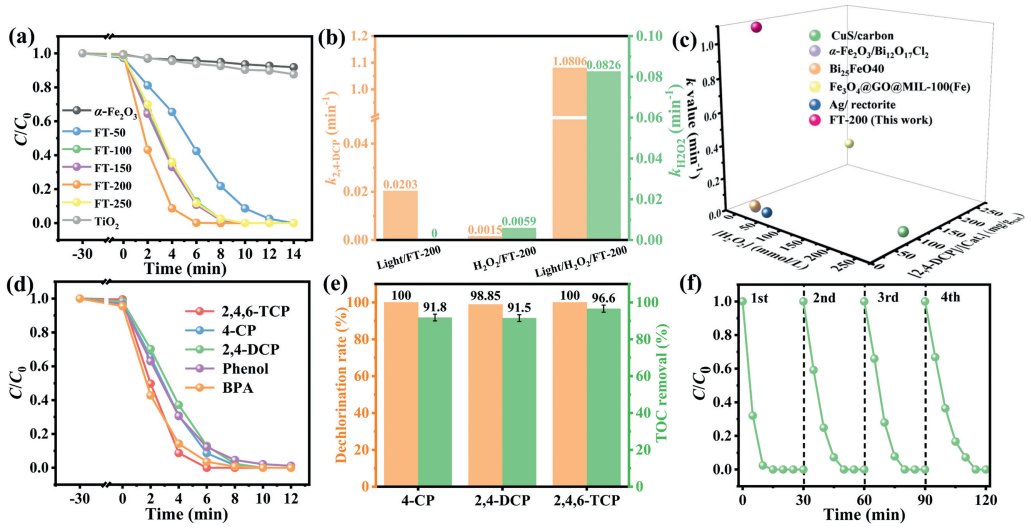

Fig. 3. (a) Photo-Fenton degradation curves of 2,4-DCP by TiO_2, α-Fe_2O_3 and FT-200. (b) *K* values of 2,4-DCP degradation and H_2O_2 decomposition in different systems. (c) Comparison of degradation performance of 2,4-DCP by different photocatalysts. (d) Effect of FT-200 on degradation of different pollutants. (e) Dechlorination and TOC removal ratios of 4-CP, 2,4-DCP and 2,4,6-TCP by Light/H_2O_2/FT-200 system. (f) Recycles test for photo-Fenton 2,4-DCP degradation by FT-200.

sulted from two respects. On the one hand, the degradation products of 2,4-DCP included some small organic acids. On the other hand, the free chloride ions were negative charged, which need proton to keep the charge balance. The coexisting ions (Cl^-, SO_4^{2-}, NO_3^-) and small molecular organic acids (maleic acid (MA), citric acid (CA), tannin acid (TA), humic acid (HA)) exhibited little inhibition on 2,4-DCP degradation, indicating the excellent resistance to salinity and coexisting organics (Fig. S10 in Supporting information). The 2,4-DCP degradation in real water was also investigated (Fig. S11 in Supporting information). Only a weak suppression could be found in both trap water and Yangtze river water, possibly due to the coexisting natural organic matters, ions or bacteria.

The stability of FT-200 was evaluated by recycling experiments. After 4 cycles of reuse, the 2,4-DCP degradation ratio maintained 100% within 30 min (Fig. 3f), and the Fe-leaching concentration during every cycle was lower than 0.6 mg/L (Fig. S12 in Supporting information). In addition, the structure variation of FT-200 before and after reaction were further investigated by XRD and XPS (Fig. S13 in Supporting information). There were no obvious differences in the XRD pattern and Fe 2p XPS spectrum of recycled FT-200 compared with that of fresh FT-200, demonstrating that the good stability and excellent reuse performance.

The leading active species in Light/H_2O_2/FT-200 system was identified by quenching experiments, with tertiary butanol (TBA), potassium thiocyanate (KSCN), β-carotene and superoxide dismutase (SOD) as the scavengers of $^{\bullet}OH$, $^1O_2$ and $^{\bullet}O_2^-$, respectively [32,33]. As shown in Figs. 4a and b, in the presence of TBA, β-carotene and SOD, the degradation ratios of 2,4-DCP decreased from 100% to 14.3%, 91.1%, and 89.4% within 12 min, respectively, indicating the dominant contribution of $^{\bullet}OH$ to 2,4-DCP degradation. In D_2O, $^1O_2$ exhibited higher life time and higher catalytic activity. As showed in Fig. S14a (Supporting information), degradation experiment of 2,4-DCP was conducted on 50% D_2O by Light/H_2O_2/FT-200 system. There was no enhanced effect after the addition of D_2O, excluding the effect of $^1O_2$. As shown in Fig. S14b (Supporting information), Light/H_2O_2/FT-200 system exhibited the highest EPR intensity of DMPO-$^{\bullet}O_2^-$ adducts, while the simple Light/FT-200 system exhibited negligible ESR intensity of DMPO-$^{\cdot}O_2^-$ adducts. Hence, the production of $^{\bullet}O_2^-$ by Light/H_2O_2/FT-200 system might be attributed to the H_2O_2 oxidation on TiO_2 surface [34]. To further identify the activation site

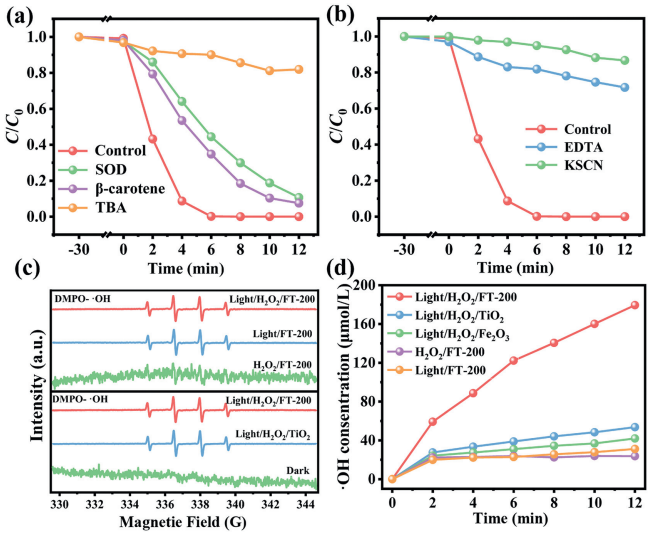

Fig. 4. (a) 2,4-DCP degradation curves in the presence of different scavengers by Light/H_2O_2/FT-200 system. (b) Effect of EDTA and KSCN on the degradation of 2,4-DCP by Light/H_2O_2/FT-200 system. (c) The EPR spectra of DMPO-$^{\bullet}OH$ in the different systems. (d) Plots of $^{\bullet}OH$ concentration as the function of time in different systems.

for H_2O_2, potassium thiocyanate (KSCN) and ethylenediaminetetraacetic acid disodium (EDTA-2Na) was injected into the photo-Fenton system, and a sharply suppression could be observed, indicated that H_2O_2 was activated at the Fe sites of α-Fe_2O_3. The production of $^{\bullet}OH$ in different reaction systems were also monitored by EPR technique. As shown in Fig. 4c, the EPR signal intensity of DMPO-$^{\bullet}OH$ adduct for Light/H_2O_2/FT-200 system was much higher than that of Light /FT-200 and H_2O_2/FT-200 system, which indicated that the photocatalysis and Fenton-like process showed synergistic effect in $^{\bullet}OH$ production. In addition, the EPR signal intensity of DMPO-$^{\cdot}OH$ adduct for Light/H_2O_2/FT-200 system was also higher than that of Light/H_2O_2/TiO_2 system, which indicated that the construction of heterojunction could enhance H_2O_2 activation and $^{\bullet}OH$ production. Subsequently, the accumulated concentration and steady concentration of $^{\bullet}OH$ production in different reaction systems was further measured (Fig. 4d and Table S4 in Supporting information). The highest $^{\bullet}OH$ accumulated concentra-

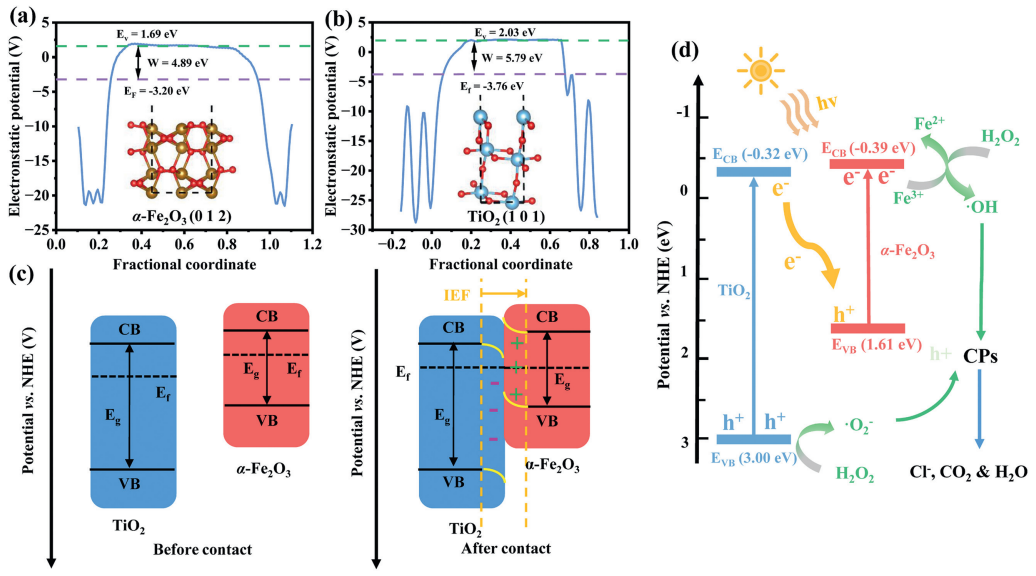

Fig. 5. The work functions of (a) α-Fe_2O_3 (012) and (b) TiO_2 (101). (c) Direct Z-scheme charge migration mechanism of α-Fe_2O_3/TiO_2 heterojunction. (d) Schematic illustration of photo-Fenton mechanism with α-Fe_2O_3/TiO_2 as catalyst under light irradiation.

tion reached 179.50 μmol/L within 12 min for Light/H_2O_2/FT-200 system, exceeding that of Light/H_2O_2/TiO_2 and Light/H_2O_2/Fe_2O_3 systems by 2.35 and 3.28 times, respectively, confirming the synergistic effect of TiO_2 and α-Fe_2O_3. Meanwhile, the ·OH accumulated concentration for Light/H_2O_2/FT-200 system was 6.58 and 4.77 times higher than that of Fenton-like and photocatalytic process, respectively, certifying the synergistic effect of H_2O_2 and light irradiation. The Light/H_2O_2/FT-200 system also exhibited the highest steady concentration of ·OH. In addition, the utilization ratio of H_2O_2 for Light/H_2O_2/FT-200 system was calculated to be 28.79%.

Meanwhile, theoretical calculations were carried out to investigate the formation of direct Z-scheme α-Fe_2O_3/TiO_2 heterojunction. The work functions were calculated based on constructed models of α-Fe_2O_3 (012) and TiO_2 (101), according to the HRTEM images in Fig. 1e. As shown in Figs. 5a and b, the work functions of α-Fe_2O_3 (012) and TiO_2 (101) were calculated as 4.89 and 5.79 eV, respectively. When α-Fe_2O_3 contacted with TiO_2, the surface electrons would transfer from α-Fe_2O_3 to TiO_2 until the Fermi levels were aligned. The internal electric field (IEF) was then built at the interface, with the energy band edges of α-Fe_2O_3 and TiO_2 bending upwards and downwards (Fig. 5c), respectively. And then, the Z-scheme carriers transfer mechanism was established in Fig. 5d under light irradiation. Driven by IEF and energy band bending, the e^- in the CB of TiO_2 recombined with the h^+ in the VB of α-Fe_2O_3 through the interface. Therefore, the e^- in the CB of α-Fe_2O_3 with strong reducibility could efficiently reduce ≡Fe(III) to ≡Fe(II), and then triggered H_2O_2 activation to produce ·OH. The h^+ in the VB of TiO_2 with strong oxidizability participated in subsequent H_2O_2 oxidation reaction to produce $\cdot O_2^-$. The produced ·OH and $\cdot O_2^-$ could effectively mineralize 2,4-DCP into CO_2 and H_2O through dechlorination and ring opening process.

The possible degradation products of 2,4-DCP were identified based on the ultra-performance liquid chromatography mass spectrometry (UPLC-MS). There were four possible degradation pathways of 2,4-DCP, as displayed in Fig. S15 (Supporting information). In summary, under the attacking of ROS, 2,4-DCP was decomposed into small molecular organic acids *via* dichlorination, hydroxylation and ring-open reaction [35,36]. Finally, the small molecular organics were further mineralized, and produced H_2O and CO_2. The toxicity of these intermediate products was estimated by Toxicity Estimation Software Tool (T.E.S.T.) with LD^{50} for rat, LC^{50} for minnows, LC^{50} for Daphnia magna and the bioconcentration factor as toxicological indexes (Fig. S16 in Supporting information). Generally, the toxicity of most intermediates was lower than that of 2,4-DCP, which indicated that Light/H_2O_2/FT-200 system could effectively reduce the environmental risks of 2,4-DCP.

In conclusion, a direct Z-scheme 0D α-Fe_2O_3/TiO_2 heterojunction was prepared by a facile *in-situ* phase transformation method. The loading of 0D α-Fe_2O_3 nanoclusters on TiO_2 nanoparticles not only improved the visible light adsorption, but also boosted the separation efficiency of photogenerated carriers. The band alignment and internal electric field demonstrated the direct Z-scheme charge transfer mechanism. Owing to the aforementioned-advantages, FT-200 exhibited the optimal photo-Fenton degradation performance towards multiple chlorophenol pollutants under a low H_2O_2 dosage (1 mmol/L) with the degradation ratios all reaching 100% within 12 min. Overall, this work proposed a facile approach for the design and construction of highly efficient direct Z-scheme photo-Fenton systems for refractory organic wastewater treatment.

Declaration of competing interest

The authors declare that they have no known competing financial interests or personal relationships that could have appeared to influence the work reported in this paper.

Acknowledgments

This work was supported by the National Key Research and Development Program of China (No. 2023YFE0100900) and the National Outstanding Youth Science Fund Project of National Natural Science Foundation of China (No. 51522805).

Supplementary materials

Supplementary material associated with this article can be found, in the online version, at doi:10.1016/j.cclet.2024.109698.

References

[1] X.M. Xu, Y.M. Zhang, Y. Chen, et al., Proc. Natl. Acad. Sci. U. S. A. 119 (2022) e2205562119.

[2] X. Li, J. Hu, Y. Deng, et al., Appl. Catal. B: Environ. 324 (2023) 122243.
[3] Y. Ahmed, J. Lu, Z. Yuan, P.L. Bond, J. Guo, Water Res. 179 (2020) 115878.
[4] X. Tian, T. Luo, Y. Nie, et al., Environ. Sci. Technol. 56 (2022) 5542–5551.
[5] F. Li, P. Wang, M. Li, et al., Water Res. 240 (2023) 120088.
[6] C. Liu, H. Dai, C. Tan, et al., Appl. Catal. B: Environ. 310 (2022) 121326.
[7] L. Su, P. Wang, X. Ma, J. Wang, S. Zhan, Angew. Chem. Ind. Ed. 60 (2021) 21261–21266.
[8] W. Xiang, Q. Ji, C. Xu, et al., Appl. Catal. B: Environ. 285 (2021) 119847.
[9] J. Zhao, M. Ji, H. Chen, et al., Applied Catal. B: Environ. 307 (2022) 121162.
[10] X. Ruan, C. Huang, H. Cheng, et al., Adv. Mater. 35 (2023) e2209141.
[11] S. Song, H. Song, L. Li, et al., Nature Catal. 4 (2021) 1032–1042.
[12] Z. Chen, H. Chen, K. Wang, et al., ACS Catal. 13 (2023) 6497–6508.
[13] C. Hou, L. Wang, W. Zhang, et al., ACS Appl. Mater. Interfaces 15 (2023) 23124–23135.
[14] Z.H. Diao, J.C. Jin, M.Y. Zou, et al., Sep. Purif. Technol. 278 (2021) 119620.
[15] M. Shi, P. Xiao, J. Lang, C. Yan, X. Yan, Adv. Sci. 7 (2020) 1901975.
[16] J. Tang, R. Xu, G. Sui, et al., Small 19 (2023) 2208232.
[17] C. Cheng, W.H. Fang, R. Long, O.V. Prezhdo, JACS Au 1 (2021) 550–559.
[18] T. Wei, P. Ding, T. Wang, et al., ACS Catal. 11 (2021) 14669–14676.
[19] W. Chen, S. Yang, H. Liu, et al., Environ. Sci. Technol. 56 (2022) 10442–10453.
[20] Y. Zhao, C. Deng, D. Tang, et al., Nature Catal. 4 (2021) 684–691.
[21] I.M. Klein, H. Liu, D. Nimlos, A. Krotz, S.K. Cushing, J. Am. Chem. Soc. 144 (2022) 12834–12841.
[22] X. Jia, C. Wang, Y. Li, et al., Chem. Eng. J. 431 (2022) 1344041.
[23] H. Ma, Y. Liu, R. Xiong, J. Wei, Chin. Chem. Lett. 33 (2022) 1042–1046.
[24] Y. Akinaga, T. Kawawaki, H. Kameko, et al., Adv. Funct. Mater. 33 (2023) 2303321.
[25] P. Yan, Q. Ren, F. Zhong, et al., Chin. Chem. Lett. 33 (2022) 3161–3166.
[26] L. Su, P. Wang, M. Li, et al., Appl. Catal. B: Environ. 335 (2023) 122890.
[27] F. Chang, F. Wu, J. Zheng, et al., Chemosphere 210 (2018) 257–266.
[28] L. Ren, S.Y. Lu, J.Z. Fang, et al., Catal. Today 281 (2017) 656–661.
[29] Q. Gong, Y. Liu, Z. Dang, J. Hazard. Mater. 371 (2019) 677–686.
[30] Y. Chen, J. Fang, S. Lu, et al., J. Hazard. Mater. 297 (2015) 278–285.
[31] Y. Chen, R. Su, F. Wang, et al., Chemosphere 270 (2021) 129295.
[32] S. Shao, J. Cui, K. Wang, et al., ACS ES&T Engineering 3 (2023) 36–44.
[33] D. Zhang, Y. Li, P. Wang, et al., Angew. Chem. Int. Ed. 62 (2023) e202303807.
[34] Z. Wei, D. Liu, W. Wei, et al., ACS Appl. Mater. Interfaces 9 (2017) 15533–15540.
[35] Z.H. Diao, Z.Y. Lin, X.Z. Chen, et al., Chem. Eng. J. 389 (2020) 123771.
[36] Z.H. Diao, L. Yan, F.X. Dong, et al., Chem. Eng. J. 379 (2020) 122313.